THE JOURNAL OF PHYSICAL CHEMISTRY B

pubs.acs.org/JPCB Article

Facile and Controllable Growth of β-FeOOH Nanostructures on Polydopamine Spheres

Klaudia Żebrowska, Emerson Coy, Karol Synoradzki, Stefan Jurga, Pau Torruella, and Radosław Mrówczyński*

Cite This: J. Phys. Chem. B 2020, 124, 9456–9463 Read Online

ACCESS | Metrics & More | Article Recommendations | Supporting Information

ABSTRACT: Polydopamine (PDA) has a wide range of applications in biomedicine due to its high biocompatibility and surface chemistry and because of the presence of many functional groups in it, enabling further modification. As a catechol-like material, it has chelation properties for various types of metal ions, including iron. Here, we developed a procedure that uses PDA as a template to grow iron structures β-FeOOH directly on its surface. The innovative approach of this work relies on that these structures can be obtained in neutral conditions and selective iron-ion source. The influence of iron-ion source, environment, and solution concentration on the structure and amount of resulting material is presented. The growth has been characterized over time, taking into account their photothermal, magnetic, and colloidal stability properties. Moreover, we shed new light on understanding the interaction of PDA with iron ions for the growth of iron-based nanostructure on polydopamine particles. Finally, we predict that PDA@β-FeOOH nanoparticles could be a promising material in dual therapy merging photothermal therapy (PTT) treatment and magnetic resonance imaging (MRI) contrast agents.

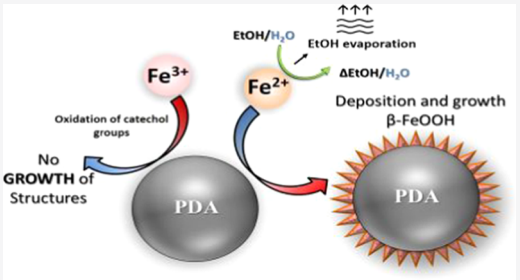

INTRODUCTION

More than 10 years ago, Lee et al. introduced a unique and versatile adhesive coating—polydopamine (PDA) that mimics mussels, which can stick through their abyssal threads to almost all types of surfaces regardless of their nature.[1−3] The research on the adhesive protein identified in the mussels foot proteins showed that they were mostly composed of amino acids, rich in catechol and amine groups.[4] This led to the conclusion that both catechol and amine groups are essential in forming adhesive layers. As a result, dopamine, present in the structure both moieties, was applied as a versatile building block for spontaneous deposition of thin polymer films.[1,5] The PDA layers, films, and particles are obtained through self-assembly and oxidative cross-linking from weakly basic solutions in a couple of hours.[6−9] This results in a robust, uniform shell of polydopamine with nanometric scale.[10−12] Moreover, the polydopamine particles size can be tuned by time, reaction medium, and pH, yielding particles from ∼40 nm to more than 200 nm.[13−15]

Materials coated with PDA, and its particles, have been used in a vast range of applications including nanomedicine, energy storage and production, tissue engineering, catalysis, flame-retardant materials preparation, and antibacterial materials.[16−26] The widespread interest in polydopamine-based materials is due to its high biocompatibility, easy functionalization with amines and sulfur-bearing moieties, and low cyto- and genotoxicity.[27] Furthermore, the PDA chelation properties resulting from the catechol group are particularly utilized to deposit a layer of metals (i.e., Mg, Mn, Cu, Gd, Au, and Ag) on PDA particles and films, rendering them catalytic and antibacterial properties or allowing new contrast properties in magnetic resonance imaging (MRI).[19,28,29] Usually, metal ions make a conformal layer around PDA; however, in some cases, they can form spherical particles like Au or Ag.[19,30,31] Among several available materials, one of the most often deposited materials on the PDA surfaces is iron, which can be used as an active chemical inducing ferroptosis in cancer cells or as a contrast agent in MRI.[32,33] More importantly, catechol's chelating properties of iron ions have been studied in detail and have been shown to depend strongly on pH, number of coordination, or ring-binding type.[34] Additionally, it was shown that iron (II) and (III) could bind to the catechol groups with different coordination numbers.[35−37] Moreover, bearing in mind the oxidizing properties of catechols, it is also possible that, as a result of the reaction with iron (II) ions, oxidation of Fe ions occurs and FeOx species are formed at the surface of PDA.[38,39] Nevertheless, there is a lack of information about morphology-controlled growth of iron structures from polydopamine particles surface, which could shed new light on

Received: July 20, 2020
Revised: September 29, 2020
Published: September 29, 2020

https://dx.doi.org/10.1021/acs.jpcb.0c06627
J. Phys. Chem. B 2020, 124, 9456–9463

Table 1. ζ-Potential Values Recorded under Different Synthetic Conditions in Reaction of PDA Nanoparticles with Various Iron Sources (Reference to Figure 1)

	A	B	C	D	E	F	G	H	I
sample	PDA $FeCl_2$ 3:1	PDA $FeCl_2$ 1:1	PDA $FeCl_2$ 1:3	PDA $FeCl_2$ 1:5	PDA $FeCl_2$ 1:3 EtOH only	PDA $FeCl_2$ 1:3 H_2O only	PDA $FeCl_3$ 1:3	PDA $FeSO_4$	PDA $C_{15}H_{21}FeO_6$
ζ-potential [mV]	+16.5	+20.5	+38.0	+39.5	+21.5	−12.5	+34.0	+14.0	−23.0

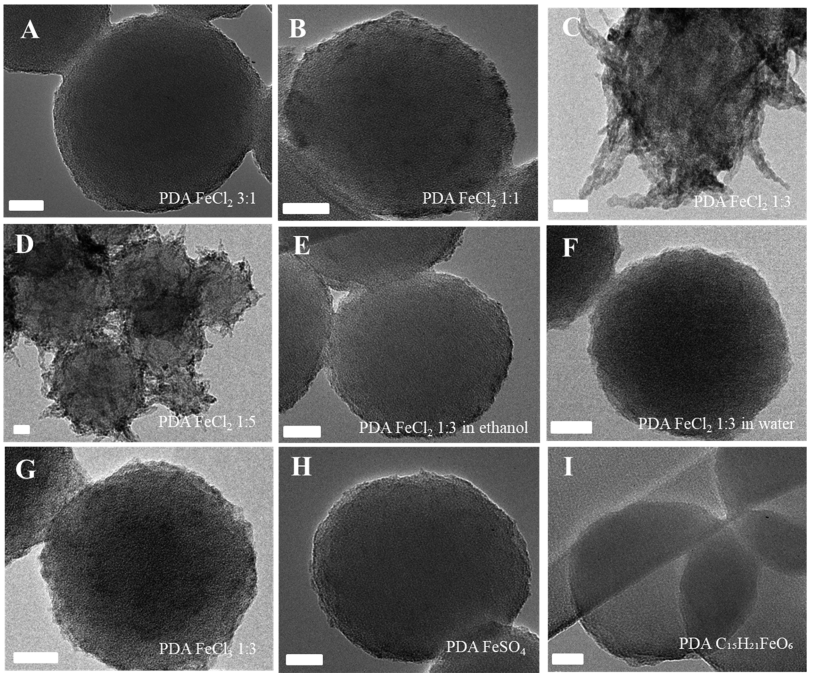

Figure 1. TEM images of PDA nanoparticles obtained under different synthetic protocols. (A) PDA/$FeCl_2$, 3:1, (B) PDA/$FeCl_2$, 1:1, (C) PDA/$FeCl_2$, 1:3, (D) PDA/$FeCl_2$, 1:5, (E) PDA/$FeCl_2$, 1:3 only in ethanol, (F) PDA/$FeCl_2$, 1:3 only in water, (G) PDA/$FeCl_3$, 1:3, (H) PDA/$FeSO_4$, (I) PDA/$C_{15}H_{21}FeO_6$. Scale bar, 20 nm.

the activity of polydopamine as an active template for new nanostructures.

Here, we present the unprecedented growth of iron hydroxide spikes directly from polydopamine particles. The obtained iron structures have nanometric size, and their growth is tailored by the reaction time, iron source, and reaction medium composition. Our process does not require initial surface modification for the synthesis of these nanostructures. Therefore, the synthesis process is straightforward and held under mild conditions. These nanostructures are characterized in detail with transmission electron microscopy (TEM), electron energy loss spectrometry (EELS), and vibrating sample magnetometry (VSM). In addition, yielded materials show also a strong photothermal response under NIR light irradiation; thus, they might serve as a potential agent for dual therapy in nanomedicine.

EXPERIMENTAL SECTION

Synthesis of PDA Nanoparticles. Dopamine hydrochloride was purchased from Alfa Aesar. The remaining chemical reagents, ethanol (99.6% purity), iron chloride (II) and (III), iron sulfate (II), iron acetylacetonate, and sodium hydroxide, were purchased from Sigma-Aldrich and used without purification. Nanoparticles with a diameter of 100 nm were obtained by dopamine polymerization under basic conditions. In a round-bottom flask, dopamine hydrochloride (200 mg, 10 mM) was dissolved in 100 mL of Milli-Q water. The solution was placed on a magnetic stirrer and heated up to 50 °C. Then, aqueous NaOH solution (0.7 mL, 1 M) was added dropwise, followed by stirring for 3 h. The particles were collected and purified by centrifugation (22 000 rpm, 20 min) and washed three times with Milli-Q water.

Iron Oxide Growth on Polydopamine Nanoparticles. To synthesize the composites, 10 mg of PDA nanoparticles in 5 mL of H_2O was added to 10 mL of EtOH in a flat-bottom flask. The flask was placed on a magnetic stirrer at room temperature (RT) followed by addition of anhydrous $FeCl_2$ (30 mg, 0.23 mM). Stirring was continued for different time intervals to monitor the growth of iron oxide. Next, the sample was purified by centrifugation (22 000 rpm, 20 min) and washed three times with Milli-Q water. To investigate the effect of medium on iron oxide growth, PDA nanoparticles suspended in water were centrifuged and washed three times with EtOH and then redispersed in 15 mL of EtOH.

Characterization Methods. Transmission electron microscopy (TEM) images were recorded on a Jeol ARM 200F high-resolution transmission electron microscope (HRTEM) and a Jeol 1400 transmission electron microscope. Samples were drop-cast on a copper grid (Formvar/Carbon 200 mesh made by Ted Pella) after 5−15 min of sonication and dried in a vacuum desiccator. Electron energy loss spectra (EELS) were collected in the same instrument, and energy loss near-edge structure (ELNES) analysis was performed in HyperSpy.[40] The electrokinetic potential was measured using a Malvern

https://dx.doi.org/10.1021/acs.jpcb.0c06627
J. Phys. Chem. B 2020, 124, 9456−9463

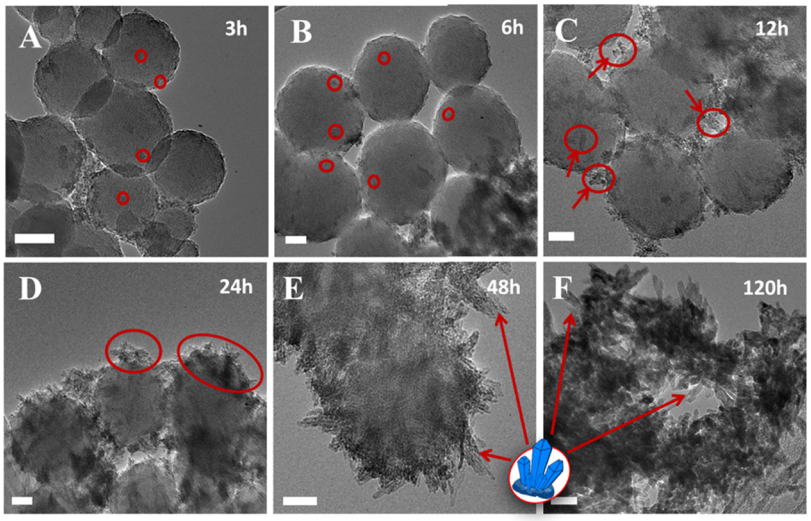

Figure 2. TEM images presenting growth of iron nanostructures on the surface of PDA in time: (A) 3 h, (B) 6 h, (C) 12 h, (D) 24 h, (E) 48 h, and (F) 120 h of iron growth. Scale bar, 20 nm.

Zetasizer Nano Series instrument. The measurements were repeated three times to ensure reproducibility. Magnetic measurements were performed with a vibrating sample magnetometer (VSM) in a physical property measurement system (PPMS) over a temperature range of 4−300 K and applied magnetic field up to 5 T. To evaluate the photothermal properties of PDA nanoparticles and PDA@β-FeOOH, they were redispersed in water in a concentration range of 10−100 μg/mL in a total volume of 1 mL. The solutions were put into a quartz cuvette (High Precision Cell cuvettes made of Quartz SUPRASIL with a 10 mm light path (Hellma Analytics)) and irradiated with an NIR laser at 808 nm wavelength and average power of 2 W/cm^2 (Changchun New Industries Optoelectronics Tech. Co., Ltd., China). The temperature of the solutions was measured by a digital thermometer with a thermocouple sensor.

RESULTS AND DISCUSSION

Synthesis and Growth. The PDA nanoparticles were obtained by oxidative polymerization of dopamine hydrochloride under alkaline conditions according to the previously reported optimized protocol.[14] The PDA nanoparticles were spherical in shape and had a diameter in the range of 90−100 nm, as determined by the TEM analysis and ζ-potential of −31 mV (Figure S1). Further, we checked the influence of the PDA-to-iron chloride (II) ratio in solution. PDA nanoparticles were mixed with $FeCl_2$ at a 3:1 ratio in the mixture of water and EtOH. The stirring was sustained for 24 h at RT. We observed a change of ζ-potential value from −31 mV for PDA nanoparticles to +16.5 mV, which suggested deposition of iron ions on the surface of PDA. Nevertheless, TEM analysis did not reveal any nanostructures on their surface. Increasing the ratio between PDA and $FeCl_2$ to 1:1 and further to 1:3 and 1:5 resulted in an increment of ζ-potential values of obtained materials up to +39 mV (see Table 1, samples B−D).

We also investigated the morphology of our materials by TEM. At the 1:1 PDA-to-$FeCl_2$ ratio, we observed deposition of small seeds around PDA nanoparticles. At higher ratios, those seeds became spikes, which grew with increased iron concentration (see Figure 1A−D). Encouraged by the obtained results, we choose 1:3 as model ratio between PDA and $FeCl_2$ to investigate the influence of reaction medium on the spike growth on PDA surfaces. For this purpose, we carried out reaction in EtOH only (see Table 1, sample E, and Figure 1E) or pure water (see Table 1, sample F, and Figure 1F). Surprisingly, under those conditions, we did not observe spikes on top of PDA nanoparticles. This showed that a mixture of both solvents was essential for the growth of those structures. However, it is worth highlighting that in the case of sample E, the ζ-potential value after reaction was higher than that in the case of sample F, which had strong negative electrokinetic potential similar to pure PDA nanoparticle. It may suggest iron ions did not deposit on PDA nanoparticles.

We also investigated the influence of iron source on the growth of spikes nanostructures. To do so, we mixed PDA nanoparticles with other inorganic salts, in particular, anhydrous $FeCl_3$ and $FeSO_4$, and an iron organic complex, iron (III) acetylacetonate. The PDA-to-iron ratio was kept at 1:3 for all cases. We did not observe spikey structures as in the case of $FeCl_2$, for any of these alternative iron sources (see Figure 1G−I). However, one has to mention that in the case of sample G, we observed a significant increase in ζ-potential to +34 mV and small seeds of iron, which did not turn into spikes. In the case of sample H, the value of ζ-potential also increased, which may indicate the presence of iron ions on the surface, however in a smaller amount. The smallest change in the ζ-potential value is observed for sample I. It means that ion deposition from iron acetylacetonate was not efficient (see Table 1, samples G−I).

Time-Dependent Growth of Spiky Nanostructures. Further, we performed an examination of iron structures growth to identify the dynamics and shape of the obtained structures. For this purpose, one sample was used and single drops were systematically taken after 3, 6, 12, 24, 48, and 120 h apart and characterized by TEM. After 3 h, there are clear darker points, which are considered as seeds, indicating the iron-ion agglomeration on the PDA nanoparticles surface (Figure 2A). However, they are not regular and occur randomly on the surface. After 6 h, the iron growth is visible (Figure 2B). After 12 h, the structure develops significantly and extends from the surface of the PDA nanoparticles (Figure 2C). It is clear that many particles have initial stages of

https://dx.doi.org/10.1021/acs.jpcb.0c06627
J. Phys. Chem. B 2020, 124, 9456−9463

development. Additionally, it is evident that the growth of the structures is not homogeneous over the entire sample. At 24 h, the particles begin to be completely covered by iron (see Figure 2D). Over time, the PDA structure was fully covered and the growth continues until the particles are saturated. At the last stages, large structures resembling crystal deposits are visible (see Figure 2E,F). It is important to note the increment of crystallinity over time; the selected area electron diffraction (SAED) patterns (see Figure 3A, inset) show the evolution of crystalline spots and the progressive disappearance of polycrystalline/amorphous rings.

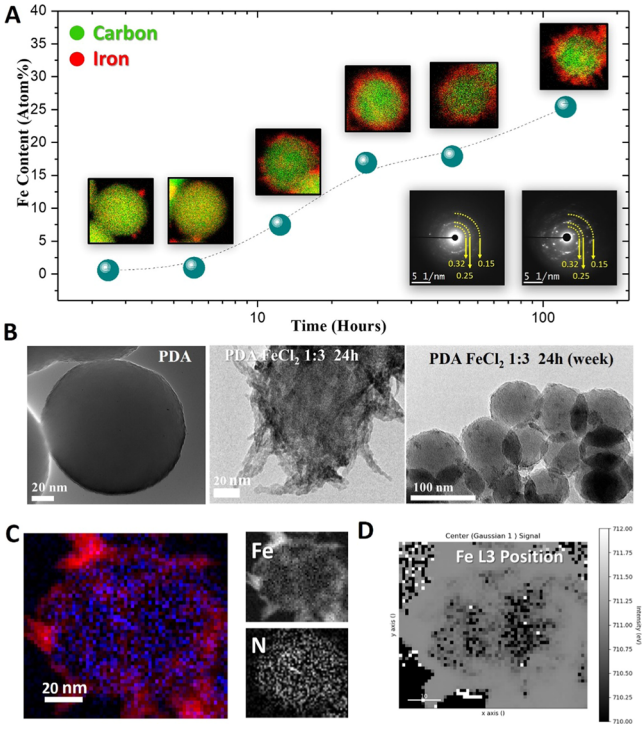

Figure 3. Graph showing the amount of iron over time from (A) 3 to 120 h with attached energy-dispersive spectroscopy (EDS) maps showing the amount of iron on the surface of PDA. SAED patterns show the increment of crystallinity of the Fe structures with time. Interplanar distance values are presented in nanometers (nm). (B) TEM images showing PDA nanoparticles, PDA with iron oxide nanostructures after 24 h synthesis and after 1 week in water. (C) Elemental distribution of a nanoparticle after 12 h, with mapping of the Fe-K edge (red) and N-K edge (blue). (D) Variation of the L3 peak position in the EELS analysis, confirming the single valence of the ion on the particle.

To estimate the concentration of iron, we perform EDS mapping measurements in TEM (see Figure 3A). It is observed that with time, iron deposition is larger and adopts a specific structure, and the increment of iron is visible in the image in red color (see Figure 3A). Further, we investigated the stability of obtained iron nanostructures on PDA nanoparticles by TEM and ζ-potential measurements. After a week of shelve storage in water, a decrease in ζ-potential was observed (see Table 2). Simultaneously, TEM imaging was performed to examine the surface of the nanoparticles, since the degradation of the iron structure could be the reason why ζ-potential changed. In fact, on the initial PDA nanoparticles modified with iron oxides spikes (synthesis of 24 h), the structures were longer visible. However, signatures of denser material and residue of iron were visible on the PDA surface (see Figure 3B).

Table 2. ζ-Potential Values for PDA Iron Nanostructures Obtained in Different Time Intervals after 1 Week in Water

time (h)	3	6	12	24	48	120	PDA
ζ-potential [mV] 1 week after synthesis	−31.0	−30.5	−26.0	−22.5	−20.0	−15.0	−31.0

Structural Identification of Iron Spikes. We have confirmed the presence of iron and the continuous growth of iron structure on the PDA surface. To get a clear picture of these aspects, EELS/ELNES measurements were performed. Iron oxide is confined to the surface of the PDA nanoparticle, as already shown by EDX, so no internal diffusion of the Fe ions is detected (see Figure 3A). Furthermore, EELS signal quantification shows the distribution of nitrogen and iron on the surface (Figure 3C). Moreover, the energy distance between the O and Fe edge remains the same and the position of the L3 peak does not change (Figure 3D). These measurements point to a single valence state for iron. After comparison of an average spectrum with reference spectra,[41] it was evaluated to be Fe^{3+}, compatible with hematite or goethite (see Figure S2). To clearly identify the crystallographic structure of the Fe nanoparticle, the collected SAED patterns, presented in Figure 3A, were further investigated. For this purpose, several electron diffraction patterns were collected from different areas of the 120 h sample and analyzed using DiffTools plugin.[42] The crystalline spots were collected and tabulated according to their interplanar distance (d) and their equivalent 2θ angle in a Cu-based diffractogram (λ = 1.5406 Å), as shown in Table S1 and Figure S3. As a result, it was determined that the Fe nanostructures grew principally as β-FeOOH, with a small quantity of γ-FeOOH.[43−47] In β-FeOOH, a chain of 4 $FeO_3(OH)_3$ octahedral is entangled to generate a nanoporous channel (<0.25 nm^2). The porous structure is partially filled by Cl^- ions, which are attracted by the H^+,[48] which is not the case for the γ-FeOOH. Thus, it is clearly shown that use of $FeCl_2$ as a precursor directly promotes the stabilization of β-FeOOH on the PDA surfaces, but in contrast, use of $FeSO_4$ promotes the growth of the γ-FeOOH phase.[46]

Photothermal Properties of PDA@β-FeOOH. Further applicability of the nanoparticle was tested based on their photothermal response. To determine such properties, PDA nanoparticles bearing β-FeOOH spikes obtained after 24, 48, and 120 h were tested (see Figures 4A and S4). They were prepared in five concentrations in the range of 10−100 μg/mL and irradiated with a laser beam with 808 nm and power of 2 W. Pure PDA spheres and water were also exposed to the same conditions as control samples (see Figure 4B). In all cases, a significant temperature medium change was obtained. The heating temperature was 40 °C for 100 μg/mL sample concentration. At the same time, the temperature change recorded for pure PDA nanoparticles at the same concentration was 10 °C lower and the water temperature increase under NIR light was around 3 °C.

Initially, no change in the amount of iron was observed on the sample after one exposure. The EDS analysis reveals that iron concentration was between 17 and 18%, which is close to the starting value of 19%. It has been reported that different iron structures can degrade between 100 and 800 °C and the weight loss was observed between 15 and 20%.[49] In our case,

https://dx.doi.org/10.1021/acs.jpcb.0c06627
J. Phys. Chem. B 2020, 124, 9456−9463

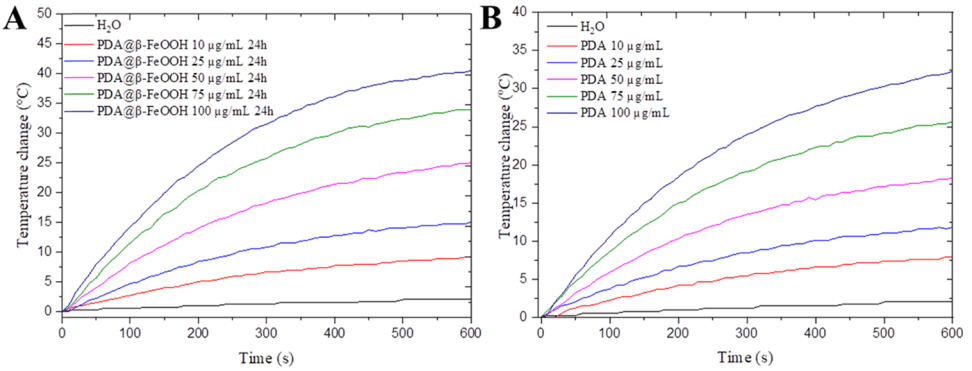

Figure 4. Photothermal properties of (A) PDA@β-FeOOH 24 h and (B) PDA, investigated for different sample concentrations.

the temperature increase at the first exposure is only 20 °C and the loss is about 1−2%.

Magnetic Characterization. An important aspect to be evaluated to assess the future applicability of the composites is their magnetic response. As an example, the results from the magnetic measurements for PDA@β-FeOOH 120 h sample are shown in Figure 5, where magnetization is determined by

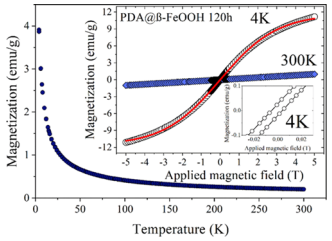

Figure 5. Temperature dependence of the zero-field-cooled (ZFC) magnetization of PDA@β-FeOOH 120 h sample measured in an applied magnetic field of 0.1 T. The inset shows magnetization curves collected at 4 and 300 K.

the total weight of the whole sample. For all tested samples, magnetization gradually increased as the temperature decreased, in a way characteristic for paramagnets. No traces of long-/short-range magnetic order or anomalies associated with the superparamagnetic effect were observed.[49] In addition, zero-field-cooled (ZFC) and FC curves overlap and no bifurcation is observed. All of this may indicate the paramagnetic properties of the materials tested. On the other hand, the value of the recorded magnetization is too high for a typical paramagnetic material (even by an order of magnitude). Pure polydopamine exhibits common paramagnetic properties, and the magnetization value does not exceed 0.12 emu/g in a 0.1 T magnetic field over the entire temperature range tested. Moreover, even for bulk β-FeOOH, the antiferromagnetic transition (which occurs around $\approx 240-299$ K[48]) is quite poorly visible. Furthermore, the relatively strong magnetic field used in our measurements (0.1 T) may have blurred this transition and made it unnoticeable. Thus, a lack of magnetic order cannot be completely excluded.

The solid red line represents the Brillouin function fit to the curve collected at 4 K. Additionally, the low field region for the curve measured at 4 K is shown. Field dependence of the magnetization $M(\mu_0 H)$ for the selected PDA@β-FeOOH sample is presented in the inset of Figure 5. $M(\mu_0 H)$ curves confirm the paramagnetic-like character of PDA@β-FeOOH 6 h, 48 h, 120 h, and PDA samples (see Figure S5). At RT, the magnetization shows linear behavior, and its value (in the limiting field of 5 T) is about ∼1 emu/g for all PDA@β-FeOOH samples. There is no hysteresis at RT. The situation changes with the decrease in temperature; at 4 K, the $M(\mu_0 H)$ curve shows an S shape and can be well described by the Brillouin function (solid line in the inset of Figure 5), which is a characteristic of paramagnets. Moreover, at this temperature, we observe a small hysteresis field $\mu_0 H_c \sim 5$ mT, which is smaller than those previously reported for nanosized β-FeOOH.[50] In the case of pure β-FeOOH nanoparticles, hysteresis may occur due to the uncompensated spin on the surface of small particles.[50,51] In the case of our samples, it cannot be ruled out that the contamination with other Fe-based compounds is the source of this behavior. The saturation magnetization at 4 K reaches 12 emu/g in a magnetic field of 5 T. This value is only slightly smaller than the one (15 emu/g) reported before for pure nanosized β-FeOOH.[50,51] In conclusion, our magnetic measurements are in good agreement with those previously presented for nanosized β-FeOOH.[50,51]

Growth Considerations and Perspectives. A few reports in the literature have shown PDA-coated substrates with similar iron structures to the ones presented here, which were obtained by incubation of $FeCl_3$ precursors in water.[52,53] However, that approach was not successful in our case. We attribute this to the very fast oxidation of catechol moieties of PDA by $FeCl_3$, which converts catechol to quinones that are not capable of chelating Fe^{2+} ions later on. Contrary to this, when initially Fe^{2+} ions are available in the reaction, they are first chelated on the surface of PDA and then seeds are formed, which enhances further growth of spiky iron oxide structure (Figure 6, left). Additionally, one key parameter in the deposition of iron nanostructures is the ethanol/water mixture. It has been observed that greater accumulation of iron ions occurs in the environment of ethanol as opposed to pure water.

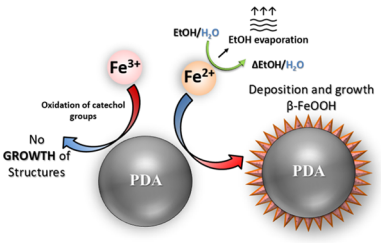

Figure 6. Schematic representation of the influence of iron valence on the growth of nanostructures and the influence of ethanol evaporation on the growth of β-FeOOH.

https://dx.doi.org/10.1021/acs.jpcb.0c06627
J. Phys. Chem. B 2020, 124, 9456−9463

This may be due to ethanol forcing the accumulation of ions on the surface of PDA nanoparticles. The presence of ethanol alone will not change the valence of iron, which is why it is not a favorable environment for them. This could be explained by two main physicochemical aspects of this mixture. First, several studies have shown that ethanol in EtOH/H_2O mixtures shows a dramatic increase in evaporation rate compared to that of ethanol alone.[54,55] Second, the solubility of $FeCl_2$ at RT in water (92 g/100 mL) and in ethanol (83 g/100 mL), which when combined with the faster evaporation rate of ethanol, would lead to a saturated environment in the mixture. The increasing and saturated water solution of iron (II) will inevitably promote the crystallization of iron nanostructures on the PDA surfaces (Figure 6, right).

Furthermore, iron ions will grow in PDA nanoparticles stored in water and then added to ethanol. The phenolic groups in polydopamine have chelation ability with a variety of metals; therefore, bidentate chelating bonding in which two oxygen atoms bound to iron might be one of the mechanisms. This can be the nucleation site from which the iron crystal structure is further formed. Nevertheless, the exact process is not identified. Many efforts have been made to clarify the structure of the PDA, but it is still not fully understood. Much less mechanism of growth is presented here, although we pose a compelling argument about the crystal anchoring on PDA surfaces. Nevertheless, these results show new possibilities for using PDA as a basis for initiating the growth of iron structures

CONCLUSIONS

We report on the facile growth of spiky nanostructures of β-FeOOH directly on polydopamine spheres. To achieve growth of β-FeOOH, $FeCl_2$ in the mixture of ethanol/water was necessary to be used for the quick evaporation of the mixture and posterior saturation of ions. The progress of the iron nanostructure growth could be followed by TEM, which revealed that structures obtained in a shorter time did not fully cover polydopamine nanoparticles and followed anchoring points. Longer reaction times above 48 h cause further growth of iron nanostructures and full covering of PDA nanoparticles. The functional tests showed that our particles were characterized by strong photothermal properties and superparamagnetic response; thus, they have potential to be applied in dual therapy merging ferroptosis and photothermal therapy (PTT) treatment, and due to their magnetic properties, as MRI contrast agents, however, those applications will be explored in further studies. In conclusion, we demonstrated the unique growth of β-FeOOH on PDA nanoparticles and investigated the dynamics growth and stability of those nanomaterials over time. Moreover, we shed new light on understanding the interaction of PDA with iron ions for the growth of iron-based nanostructures on polydopamine particles.

ASSOCIATED CONTENT

Supporting Information

The Supporting Information is available free of charge at https://pubs.acs.org/doi/10.1021/acs.jpcb.0c06627.

TEM image of PDA nanoparticles, ζ-potential value −31 mV (Figure S1), PCA EELS (Figure S2), histogram of 2θ angles (Figure S3), photothermal properties of PDA@β-FeOOH 48 h and PDA@β-FeOOH 120 h (Figure S4), additional magnetic measurements (Figure S5), and interplanar distances from SAED (Table S1) (PDF)

AUTHOR INFORMATION

Corresponding Author

Radosław Mrówczyński − *NanoBioMedical Centre, Adam Mickiewicz University in Poznan, PL-61-614 Poznan, Poland;* orcid.org/0000-0003-3687-911X; Phone: +48 61 829-6704; Email: radoslaw.mrowczynski@amu.edu.pl

Authors

Klaudia Żebrowska − *NanoBioMedical Centre, Adam Mickiewicz University in Poznan, PL-61-614 Poznan, Poland*

Emerson Coy − *NanoBioMedical Centre, Adam Mickiewicz University in Poznan, PL-61-614 Poznan, Poland;* orcid.org/0000-0002-4149-9720

Karol Synoradzki − *NanoBioMedical Centre, Adam Mickiewicz University in Poznan, PL-61-614 Poznan, Poland; Institute of Molecular Physics, Polish Academy of Sciences, 60-179 Poznan, Poland*

Stefan Jurga − *NanoBioMedical Centre, Adam Mickiewicz University in Poznan, PL-61-614 Poznan, Poland;* orcid.org/0000-0002-1665-6077

Pau Torruella − *Haldor Topsøe A/S, DK-2800 Kgs. Lyngby, Denmark*

Complete contact information is available at: https://pubs.acs.org/10.1021/acs.jpcb.0c06627

Notes

The authors declare no competing financial interest.

ACKNOWLEDGMENTS

The financial support under research grant numbers UMO-2018/31/B/ST8/02460 by The National Science Centre and POWR.03.02.00-00-I032/16 by The National Centre for Research and Development is kindly acknowledged.

REFERENCES

(1) Lee, H.; Dellatore, S. M.; Miller, W. M.; Messersmith, P. B. Mussel-Inspired Surface Chemistry for Multifunctional Coatings. *Science* **2007**, *318*, 426−430.

(2) Silverman, H. G.; Roberto, F. F. Understanding Marine Mussel Adhesion. *Mar. Biotechnol.* **2007**, *9*, 661−681.

(3) Waite, J. H.; Tanzer, M. L. Polyphenolic Substance of Mytilus Edulis: Novel Adhesive Containing L-Dopa and Hydroxyproline. *Science* **1981**, *212*, 1038−1040.

(4) Petrone, L.; Kumar, A.; Sutanto, C. N.; Patil, N. J.; Kannan, S.; Palaniappan, A.; Amini, S.; Zappone, B.; Verma, C.; Miserez, A. Mussel Adhesion Is Dictated by Time-Regulated Secretion and Molecular Conformation of Mussel Adhesive Proteins. *Nat. Commun.* **2015**, *6*, No. 8737.

(5) Ryu, J. H.; Messersmith, P. B.; Lee, H. Polydopamine Surface Chemistry: A Decade of Discovery. *ACS Appl. Mater. Interfaces* **2018**, *10*, 7523−7540.

(6) Xiong, S.; Wang, Y.; Yu, J.; Chen, L.; Zhu, J.; Hu, Z. Polydopamine Particles for Next-Generation Multifunctional Biocomposites. *J. Mater. Chem. A* **2014**, *2*, 7578−7587.

(7) Wang, X.; Chen, Z.; Yang, P.; Hu, J.; Wang, Z.; Li, Y. Size Control Synthesis of Melanin-like Polydopamine Nanoparticles by Tuning Radicals. *Polym. Chem.* **2019**, *10*, 4194−4200.

(8) Jiang, X.; Wang, Y.; Li, M. Selecting Water-Alcohol Mixed Solvent for Synthesis of Polydopamine Nano-Spheres Using Solubility Parameter. *Sci. Rep.* **2014**, *4*, No. 6070.

(9) Kohri, M. Artificial Melanin Particles: New Building Blocks for Biomimetic Structural Coloration. *Polym. J.* **2019**, *51*, 1127−1135.

(10) Li, H.; Xi, J.; Zhao, Y.; Ren, F. Mechanical Properties of Polydopamine (PDA) Thinfilms. *MRS Adv.* **2019**, *4*, 405−412.
(11) Zangmeister, R. A.; Morris, T. A.; Tarlov, M. J. Characterization of Polydopamine Thin Films Deposited at Short Times by Autoxidation of Dopamine. *Langmuir* **2013**, *29*, 8619−8628.
(12) Ball, V. Composite Materials and Films Based on Melanins, Polydopamine, and Other Catecholamine-Based Materials. *Biomimetics* **2017**, *2*, No. 12.
(13) Harvey, S.; Ng, D. Y. W.; Szelwicka, J.; Hueske, L.; Veith, L.; Raabe, M.; Lieberwirth, I.; Fytas, G.; Wunderlich, K.; Weil, T. Facile Synthesis of Ultrasmall Polydopamine-Polyethylene Glycol Nanoparticles for Cellular Delivery. *Biointerphases* **2018**, *13*, No. 06D407.
(14) Ho, C. C.; Ding, S. J. The pH-Controlled Nanoparticles Size of Polydopamine for Anti-Cancer Drug Delivery. *J. Mater. Sci.: Mater. Med.* **2013**, *24*, 2381−2390.
(15) Poinard, B.; Neo, S. Z. Y.; Yeo, E. L. L.; Heng, H. P. S.; Neoh, K. G.; Kah, J. C. Y. Polydopamine Nanoparticles Enhance Drug Release for Combined Photodynamic and Photothermal Therapy. *ACS Appl. Mater. Interfaces* **2018**, *10*, 21125−21136.
(16) Mrówczyński, R. Polydopamine-Based Multifunctional (Nano)-Materials for Cancer Therapy. *ACS Appl. Mater. Interfaces* **2018**, *10*, 7541−7561.
(17) Liu, Y.; Ai, K.; Lu, L. Polydopamine and Its Derivative Materials: Synthesis and Promising Applications in Energy, Environmental, and Biomedical Fields. *Chem. Rev.* **2014**, *114*, 5057−5115.
(18) Qu, K.; Wang, Y.; Vasileff, A.; Jiao, Y.; Chen, H.; Zheng, Y. Polydopamine-Inspired Nanomaterials for Energy Conversion and Storage. *J. Mater. Chem. A* **2018**, *6*, 21827−21846.
(19) Wang, Z.; Zou, Y.; Li, Y.; Cheng, Y. Metal-Containing Polydopamine Nanomaterials: Catalysis, Energy, and Theranostics. *Small* **2020**, *16*, No. 1907042.
(20) Pawar, S. A.; Chand, A. N.; Kumar, A. V. Polydopamine: An Amine Oxidase Mimicking Sustainable Catalyst for the Synthesis of Nitrogen Heterocycles under Aqueous Conditions. *ACS Sustainable Chem. Eng.* **2019**, *7*, 8274−8286.
(21) Mrõwczyński, R.; Bunge, A.; Liebscher, J. Polydopamine - An Organocatalyst Rather than an Innocent Polymer. *Chem. − Eur. J.* **2014**, *20*, 8647−8653.
(22) Kim, H.; Kim, D. W.; Vasagar, V.; Ha, H.; Nazarenko, S.; Ellison, C. J. Polydopamine-Graphene Oxide Flame Retardant Nanocoatings Applied via an Aqueous Liquid Crystalline Scaffold. *Adv. Funct. Mater.* **2018**, *28*, No. 1803172.
(23) Cho, J. H.; Vasagar, V.; Shanmuganathan, K.; Jones, A. R.; Nazarenko, S.; Ellison, C. J. Bioinspired Catecholic Flame Retardant Nanocoating for Flexible Polyurethane Foams. *Chem. Mater.* **2015**, *27*, 6784−6790.
(24) Wang, H.; Cao, J.; Luo, F.; Cao, C.; Qian, Q.; Huang, B.; Xiao, L.; Chen, Q. Simultaneously Enhanced Mechanical Properties and Flame Retardancy of UHMWPE with Polydopamine-Coated Expandable Graphite. *RSC Adv.* **2019**, *9*, 21371−21380.
(25) Kim, Y.; Coy, E.; Kim, H.; Mrówczyński, R.; Torruella, P.; Jeong, D.-W.; Choi, K. S.; Jang, J. H.; Song, M. Y.; Jang, D.-J.; et al. Efficient Photocatalytic Production of Hydrogen by Exploiting the Polydopamine-Semiconductor Interface. *Appl. Catal., B* **2021**, *280*, No. 119423.
(26) Fedorenko, V.; Viter, R.; Mrówczyński, R.; Damberga, D.; Coy, E.; Iatsunskyi, I. Synthesis and Photoluminescence Properties of Hybrid 1D Core−Shell Structured Nanocomposites Based on ZnO/Polydopamine. *RSC Adv.* **2020**, *10*, 29751−29758.
(27) Woźniak, A.; Walawender, M.; Tempka, D.; Coy, E.; Załęski, K.; Grześkowiak, B. F.; Mrówczyński, R. In Vitro Genotoxicity and Cytotoxicity of Polydopamine-Coated Magnetic Nanostructures. *Toxicol. In Vitro* **2017**, *44*, 256−265.
(28) Ge, R.; Lin, M.; Li, X.; Liu, S.; Wang, W.; Li, S.; Zhang, X.; Liu, Y.; Liu, L.; Shi, F.; et al. Cu^{2+}-Loaded Polydopamine Nanoparticles for Magnetic Resonance Imaging-Guided pH- and near-Infrared-Light-Stimulated Thermochemotherapy. *ACS Appl. Mater. Interfaces* **2017**, *9*, 19706−19716.
(29) Guo, H.; Sun, H.; Zhu, H.; Guo, H.; Sun, H. Synthesis of Gd-Functionalized Fe_3O_4@polydopamine Nanocomposites for: T1/T2 Dual-Modal Magnetic Resonance Imaging-Guided Photothermal Therapy. *New J. Chem.* **2018**, *42*, 7119−7124.
(30) Wu, C.; Zhang, G.; Xia, T.; Li, Z.; Zhao, K.; Deng, Z.; Guo, D.; Peng, B. Bioinspired Synthesis of Polydopamine/Ag Nanocomposite Particles with Antibacterial Activities. *Mater. Sci. Eng., C* **2015**, *55*, 155−165.
(31) Zeng, T.; Zhang, X. Le.; Niu, H. Y.; Ma, Y. R.; Li, W. H.; Cai, Y. Q. In Situ Growth of Gold Nanoparticles onto Polydopamine-Encapsulated Magnetic Microspheres for Catalytic Reduction of Nitrobenzene. *Appl. Catal., B* **2013**, *134*−*135*, 26−33.
(32) Chen, L.; Lin, Z.; Liu, L.; Zhang, X.; Shi, W.; Ge, D.; Sun, Y. Fe^{2+}/Fe^{3+} Ions Chelated with Ultrasmall Polydopamine Nanoparticles Induce Ferroptosis for Cancer Therapy. *ACS Biomater. Sci. Eng.* **2019**, *5*, 4861−4869.
(33) Guan, Q.; Guo, R.; Huang, S.; Zhang, F.; Liu, J.; Wang, Z.; Yang, X.; Shuai, X.; Cao, Z. Mesoporous Polydopamine Carrying Sorafenib and SPIO Nanoparticles for MRI-Guided Ferroptosis Cancer Therapy. *J. Controlled Release* **2020**, *320*, 392−403.
(34) Andjelković, M.; Van Camp, J.; De Meulenaer, B.; Depaemelaere, G.; Socaciu, C.; Verloo, M.; Verhe, R. Iron-Chelation Properties of Phenolic Acids Bearing Catechol and Galloyl Groups. *Food Chem.* **2006**, *98*, 23−31.
(35) Yamahara, R.; Ogo, S.; Masuda, H.; Watanabe, Y. (Catecholato)Iron(III) Complexes: Structural and Functional Models for the Catechol-Bound Iron(III) Form of Catechol Dioxygenases. *J. Inorg. Biochem.* **2002**, *88*, 284−294.
(36) Xu, Z. Mechanics of Metal-Catecholate Complexes: The Roles of Coordination State and Metal Types. *Sci. Rep.* **2013**, *3*, No. 2914.
(37) Sundaravel, K.; Dhanalakshmi, T.; Suresh, E.; Palaniandavar, M. Synthesis, Structure, Spectra and Reactivity of Iron(III) Complexes of Facially Coordinating and Sterically Hindering 3N Ligands as Models for Catechol Dioxygenases. *Dalton Trans.* **2008**, 7012−7025.
(38) Yan, J.; Yang, L.; Lin, M. F.; Ma, J.; Lu, X.; Lee, P. S. Polydopamine Spheres as Active Templates for Convenient Synthesis of Various Nanostructures. *Small* **2013**, *9*, 596−603.
(39) Zhang, M.; He, X.; Chen, L.; Zhang, Y. Preparation of IDA-Cu Functionalized Core-Satellite Fe_3O_4/Polydopamine/Au Magnetic Nanocomposites and Their Application for Depletion of Abundant Protein in Bovine Blood. *J. Mater. Chem.* **2010**, *20*, 10696−10704.
(40) Peña, F.; de la Ostasevicius, T.; Fauske, V. T.; Burdet, P.; Jokubauskas, P.; Nord, M.; Prestat, E.; Sarahan, M.; MacArthur, K. E.; Johnstone, D. N. et al. *HyperSpy 1.3*; 2017.
(41) Ewels, P.; Sikora, T.; Serin, V.; Ewels, C. P.; Lajaunie, L. A Complete Overhaul of the Electron Energy-Loss Spectroscopy and X-Ray Absorption Spectroscopy Database: Eelsdb.Eu. *Microsc. Microanal.* **2016**, *22*, 717−724.
(42) Mitchell, D. R. G. DiffTools: Electron Diffraction Software Tools for DigitalMicrograph. *Microsc. Res. Tech.* **2008**, *71*, 588−593.
(43) Song, H.; Zhang, X.; Chen, T.; Jia, X. One-Pot Synthesis of Bundle-like β-FeOOH Nanorods and Their Transformation to Porous α-Fe_2O_3 Microspheres. *Ceram. Int.* **2014**, *40*, 15595−15602.
(44) Geng, F.; Zhao, Z.; Geng, J.; Cong, H.; Cheng, H. M. A Simple and Low-Temperature Hydrothermal Route for the Synthesis of Tubular α-FeOOH. *Mater. Lett.* **2007**, *61*, 4794−4796.
(45) Xiao, H.; Ye, W.; Song, X.; Ma, Y.; Li, Y. Evolution of Akaganeite in Rust Layers Formed on Steel Submitted to Wet/Dry Cyclic Tests. *Materials* **2017**, *10*, No. 1262.
(46) Zhou, Q.; Wu, W.; Zhou, S.; Xing, T.; Sun, G.; Chen, G. Polydopamine-Induced Growth of Mineralized γ-FeOOH Nanorods for Construction of Silk Fabric with Excellent Superhydrophobicity, Flame Retardancy and UV Resistance. *Chem. Eng. J.* **2020**, *382*, No. 122988.
(47) Domingo, C.; Rodriguez-Clemente, R.; Blesa, M. Morphological Properties of α-FeOOH, γ-FeOOH and Fe3O4 Obtained by Oxidation of Aqueous Fe(II) Solutions. *J. Colloid Interface Sci.* **1994**, *165*, 244−252.

https://dx.doi.org/10.1021/acs.jpcb.0c06627
J. Phys. Chem. B 2020, 124, 9456−9463

(48) Suzuki, T. M.; Nonaka, T.; Suda, A.; Suzuki, N.; Matsuoka, Y.; Arai, T.; Sato, S.; Morikawa, T. Highly Crystalline β-FeOOH(Cl) Nanorod Catalysts Doped with Transition Metals for Efficient Water Oxidation. *Sustainable Energy Fuels* **2017**, *1*, 636−643.
(49) Sayed, F. N.; Polshettiwar, V. Facile and Sustainable Synthesis of Shaped Iron Oxide Nanoparticles: Effect of Iron Precursor Salts on the Shapes of Iron Oxides. *Sci. Rep.* **2015**, *5*, No. 9733.
(50) Veverka, P.; Pashchenko, M.; Kubíčková, L.; Kuličková, J.; Jirák, Z.; Havelek, R.; Královec, K.; Kohout, J.; Kaman, O. Rod-like Particles of Silica-Coated Maghemite: Synthesis via Akaganeite, Characterization and Biological Properties. *J. Magn. Magn. Mater.* **2019**, *476*, 149−156.
(51) Urtizberea, A.; Luis, F.; Millán, A.; Natividad, E.; Palacio, F.; Kampert, E.; Zeitler, U. Thermoinduced Magnetic Moment in Akaganéite Nanoparticles. *Phys. Rev. B* **2011**, *83*, No. 214426.
(52) Zhang, C.; Yang, H.-C. C.; Wan, L.-S. S.; Liang, H.-Q. Q.; Li, H.; Xu, Z.-K. K. Polydopamine-Coated Porous Substrates as a Platform for Mineralized β-FeOOH Nanorods with Photocatalysis under Sunlight. *ACS Appl. Mater. Interfaces* **2015**, *7*, 11567−11574.
(53) Cheng, D.; Zhang, Y.; Bai, X.; Liu, Y.; Deng, Z.; Wu, J.; Bi, S.; Ran, J.; Cai, G.; Wang, X. Mussel-Inspired Fabrication of Superhydrophobic Cotton Fabric for Oil/Water Separation and Visible Light Photocatalytic. *Cellulose* **2020**, *27*, 5421−5433.
(54) Innocenzi, P.; Malfatti, L.; Costacurta, S.; Kidchob, T.; Piccinini, M.; Marcelli, A. Evaporation of Ethanol and Ethanol-Water Mixtures Studied by Time-Resolved Infrared Spectroscopy. *J. Phys. Chem. A* **2008**, *112*, 6512−6516.
(55) O'Hare, K. D.; Spedding, P. L.; Grimshaw, J. Evaporation of the Ethanol and Water Components Comprising a Binary Liquid Mixture. *Dev. Chem. Eng. Miner. Process.* **1993**, *1*, 118−128.

https://dx.doi.org/10.1021/acs.jpcb.0c06627
J. Phys. Chem. B 2020, 124, 9456−9463